Wing pitch timing and wing elevation modulate forces and body pitch in forward flapping flight

Authors: Victor Colognesi[†] and L. Christoffer Johansson[†]

Author affiliations: [†] Biology department, Lund University, 223 62 Lund, Sweden

ORCID: V.C. 0000-0003-4109-8174, L.C.J. 0000-0002-1851-3635

Author Contributions: V.C. and L.C.J. conceived and planned the study and conducted the experiments. V.C. performed the PIV and data analysis and drew the associated figures. L.C.J. conducted the statistical analyses and drafted the manuscript. Both authors participated in finalizing the text and figures.

Contact information: V. C. victor.colognesi@biol.lu.se, LCJ Christoffer.Johansson@biol.lu.se

Competing Interest Statement: The authors have no competing interests.

Scientific fields: Biological Sciences/Evolution, Biomechanics, Physical Sciences/Physics, Aerodynamics

Keywords: Animal flight, aerodynamics, flight efficiency, robotic flapping wing, pitch control, kinematics, drones, tailless flight control

Abstract

Aerodynamic performance in airplanes and flying animals can be controlled by changes in wing shape and size, but during flapping flight another key component is wing motion. Observations of free-flying animals reveal natural wing motions, but testing causal mechanisms requires controlled manipulation of flapping kinematics. In flapping wings, aerodynamic interactions between the two wings are expected to depend on wingbeat phase, wing proximity, and wing attitude. How these interactions influence force production remains unclear. Here we used a robotic flapping wing and quantitative flow measurements to test the effect of wing interactions between wings flapped above or below the body in combination with pitch timing during upstroke–downstroke transitions. We show that both force magnitude and direction depend strongly on these parameters. High wing position combined with early pitching enhanced vertical force, whereas low position and late pitching increased thrust. Maximum aerodynamic efficiency was achieved flapping around the horizontal plane and pitching late. Transition phases strongly affected thrust generation and produced substantial body pitch torques. These findings demonstrate that small kinematic adjustments can markedly alter aerodynamic performance and be used for tailless flight control. This offers mechanistic explanations for observed animal wing motions and novel strategies for controlling flapping drones.

Introduction

Animals in flapping flight regulate both the magnitude and direction of aerodynamic forces through passive wing deformations and active muscular control. Birds, bats, and insects continually adjust wing trajectory, attitude, and velocity to maintain stability (1), modulate speed (2–8), and execute maneuvers (9–12). Variations in kinematics can disproportionately influence both the magnitude and orientation of aerodynamic forces (13,14), thereby shaping flight performance across speeds, accelerations, and environmental conditions. This flexibility arises from the biological flight apparatus, which allows for virtually infinite kinematic variation. Understanding how specific wing-motion parameters affect force generation is therefore critical both for explaining the diversity of natural flight behaviors and for guiding the design of the next generation flapping-wing robots (15).

Despite major advances in animal-flight research (16–20), the aerodynamic consequences of most kinematic variation remain unresolved. The link between kinematics and aerodynamics is relatively well understood for hovering flight (14,21–24), while prior work on forward-flight remains more limited. Work on forward flapping flight has primarily examined parameters such as Strouhal number (flapping velocity relative to forward speed) (25) and wing pitch amplitude (26), or simplified flapping to heaving wings (27,28), which is insufficient to capture the 3D flow phenomena of flapping wings (29). However, studies of hovering flight dynamics and theoretical reasoning suggest additional strategies to control aerodynamics, which may apply to forward flight but remain largely unexplored. Indeed, recent experiments showed that mean wing elevation, a previously untested parameter, can modulate both force magnitude and orientation by altering wing-wing interactions during the downstroke (30). Another particularly potent parameter to control forces is pitch timing, which influences the angle of attack and wing-wake interactions in hovering-flight studies (14,31,32). In forward-flying animals, pitch timing and mean wing elevation have rarely been explicitly studied (but see (33) for a 2D study), although available evidence suggest that the parameters vary with flight speed in flying animals (4,8,34–39). However, the mechanistic links between these kinematic parameters and the resulting aerodynamic forces are difficult to isolate in vivo. A systematic, computational or robot-based experimental analysis is therefore needed to disentangle how variation in wing kinematic parameters influences the balance between lift and thrust and the efficiency with which these forces are produced.

Here, we address this knowledge gap by experimentally quantifying how wing pitch timing and mean wing elevation interact to shape aerodynamic performance using a robotic flapping wing. Using a wind tunnel setup with particle image velocimetry (PIV) to measure airflow, we independently manipulate wing pitch timing and mean wing elevation and quantify the resulting lift, thrust, force orientation, and energetic costs. This approach isolates how these parameters alter aerodynamic output, offering a mechanistic framework for interpreting kinematic variability in flying animals. By revealing how targeted timing and positional adjustments regulate aerodynamic forces, our findings offer new insights into natural flight control and inform strategies for achieving robust, responsive, and energy efficient control in flapping drones.

Material and methods

We used a robot (previously described in (30,40)), fitted with a novel 3D-printed wing (wing length = 150 mm, mean chord = 39 mm, maximum thickness = 6 mm, see Fig. S1). The robot is capable of independently controlling the angular elevation of the wing above (max 90 degrees) and angular depression of the wing below (max 90 degrees) the horizontal plane through the flapping axis, the wingbeat frequency (*f*, in the range 0-15 Hz) and the pitch angle (γ, varying ±40 degrees). These factors can be controlled as continuous functions over time and essentially take any shape allowed by motor acceleration. Here we controlled the mean wing elevation (*MWE*) and the pitch angle (γ). *MWE* was defined as the average of the maximum elevation and depression angles of the wing relative to the horizontal flapping plane. Positive values represent wingbeats centered above the horizontal, negative below. Pitch angle was defined as the angular rotation of the wing around the spanwise axis. The robot was mounted on the wall of the wind tunnel and was controlled using a custom software via a microcontroller (30,40).

For the experiments we used fixed tunnel speed (7.2 m/s), tip-to-tip angular amplitude of the flapping (A_{ang} = 70 degrees), flapping frequency (6.7 Hz) and downstroke ratio (0.5, equal duration of down and upstroke). For all experiments, the wing flaps at a constant velocity and constant pitch for the downstrokes (-4 degrees), and upstrokes (14 degrees). At the transitions, both the velocity and the pitch follow a sinusoidal trajectory, taking 10% of the total flapping period and ensuring a continuous and smooth transition. The timing of the pitch (*TP*) transition was then shifted according to three scenarios, with a delay of minus half of the transition time (so -5% of the period), 0 and plus half of the transition time (Fig. S2). An 'early' pitch means the wing rotates before reaching the turning point, while a 'late' pitch means rotation occurs after the turning point. We varied the *MWE* (by independently controlling the maximum elevation and depression angle of the wing) between -30 deg (low), 0 deg (mid) and 30 deg (high). For each kinematic condition, we made three measurements, where each measurement included four flapping cycles. The wing motion was stopped between each measurement and subsequently started again providing unique starting conditions for the wing for each sequence. We therefore considered the measurements to be statistically independent.

We defined a right-handed coordinate system with *x* in the tunnel flow direction and *z* in the upwards direction. We measured the flow using stereo particle image velocimetry (sPIV) in a plane perpendicular to the freestream flow (*yz*-plane) of the Lund University wind tunnel (41). The sPIV system (Lavision, Göttingen, Germany) includes a dual pulse laser (LDY304PIV laser, Litron Lasers, Rugby, England), operated at f_L=720 Hz, four high speed cameras (Photron Nova R2, Photron Deutschland GmbH, Reutlingen, Germany) and acquisition and analysis software (Davis 10.2.1, Lavision, Göttingen, Germany). The cameras were set up to all view the same area (~340 x 400 mm, *yz*). The analysis settings were; pre-processing with a subtract minimum over time (5 frames), followed by a vector calculation with an initial box size of 96x96 and a final box size of 24x24, with 50% overlap. The final vector field, with a vector spacing of 3.8 mm (~2.6 vectors/cm), was subjected to a vector validation of strength 2. To remove erroneous vectors and noise we did a final post processing step. This included a 1x universal outlier detection, removing vectors deviating more than 2.5 standard deviation from their neighbors (7x7 box) and reinserting the second-best vector if less than 3 standard deviations from their neighbors. This step also included interpolating

missing vectors and a 5x5 denoising routine. The resulting vector field was 150x177 vectors with a spacing of 2.27 mm.

The vector fields were analyzed using custom written software in Matlab R2022a (Mathworks Inc.). The data were masked to remove erroneous vectors at the edge of the vector field and mirrored in the sagittal plane of the robot, to generate a wake representing both wings of an animal. Mirroring the vector field is motivated by the wind tunnel wall acting as an aerodynamic mirror (42–45), making it possible to study wing-wing interactions using a single wing (44). This procedure ignores effects of the boundary layer but given that the boundary layer in the current tunnel is thin (46) and that all measurements are performed at the same speed we consider these effects to be small.
In each PIV sequence, the free-stream velocity U_∞ was estimated by averaging the measured streamwise velocity in an area unaffected by the wake of the wing. We then stacked the vector fields in the streamwise direction with a spacing of U_∞/f_L and estimated the vorticity (ω, a measure of the rotation of the flow) as the curl of the flow velocities in the volume.
The vertical force, lift (L), was calculated according to,

$$L = \rho U_\infty \iint_{wake\ area} (y - y_0) \cdot \omega_x(y,z)\, dydz \quad (1)$$

where ρ is the air density, y is the spanwise position, y_0 the spanwise position of the center of the body and ω_x is the vorticity along the freestream axis.
We estimated the thrust (T) in the direction of flight as,

$$T = \frac{1}{2}\rho U_\infty \iint_{wake\ area} (y - y_0) \cdot \omega_z(y,z) - (z - z_0) \cdot \omega_y(y,z)\, dydz \quad (2)$$

where ω_z is the vorticity along the vertical axis, ω_y is the vorticity along the spanwise axis, z the vertical position and z_0 the vertical position of the center of the body (47).
For the comparisons in this paper, we used the time-averaged force over four wingbeats. The direction of the resultant force was determined as the average thrust to average lift ratio (T/L) and the ability to generate force was determined by estimating the force coefficients,

$$C_L = \frac{L}{\mathrm{qS}} \quad (3)$$

$$C_T = \frac{T}{\mathrm{qS}} \quad (4)$$

where q is the dynamic pressure ($q = \frac{1}{2}\rho U_\infty^2$) and S is the wing area.
We also estimated the useful force (F_{use}) as the magnitude of the vector sum of T and L and normalized according to,

$$C_{Fuse} = \frac{F_{use}}{\mathrm{qS}}. \quad (5)$$

We determined the kinetic energy in the wake as a measure of the cost of generating the forces (48,49), using the following equation:

$$E = \frac{1}{2}\rho \int_{Wake\ volume} (2uU_\infty + u^2 + v^2 + w^2) \cdot \left(1 + \frac{u}{U_\infty}\right) dV \text{ (6)},$$

where *u*, *v*, *w* are the induced velocities in *x*, *y*, *z*, respectively. Contrarily to the vorticity field, which is compact, the velocity field is not captured in its entirety by the PIV measurements. To improve our estimation of the kinetic energy, we performed a Helmholtz-Hedge decomposition and extended the velocity field beyond the dimensions of the wind tunnel (here to a size of 1.2 x 1.2 m cross section) (48,49).

The reconstruction is based on a masked vorticity field. The mask was generated automatically from the data. It started with the large vortical structures, then included a set volume around them. The final mask applied to the 3D vorticity field was an extrusion of a 2D mask normal to the flow direction obtained by combining all 2D slices of the initial 3D mask. Due to the flow field being reconstructed from the vorticity based on the stacked 2D-slices of the flow, velocity at the edges of the volume did not always become zero. We therefore subtracted the mean streamwise velocity at the edges of the volume before calculating the kinetic energy.

The first term in the energy equation is related to the momentum change due to non-zero thrust production by the wing. While it vanishes for flying objects at force equilibrium this term is necessary to account for the net forces generated by the wing (50). Assuming no pressure work on the Treftz plane, the power was subsequently estimated by dividing the kinetic energy in the wake by the number of wingbeats (N_{wb}= 4) and multiplying by the wingbeat frequency (*f*):

$$P = \frac{E}{N_{wb}} f \text{ (7)}.$$

We then normalized power by calculating the power coefficient (C_P) as,

$$C_P = \frac{P}{qS\ \ \infty}. \text{ (8)}$$

Since the force generation differs between the kinematic settings, we estimated performance parameters to allow for a comparison between the cases. A traditional measure of performance is the cost of transport (COT), a measure of the relative cost of generating *L*, defined as the energy required to transport one unit of weight, one unit of distance. By equating the weight with the lift generated by the wing COT becomes:

$$COT = \frac{P}{LU_\infty}. \text{ (9)}$$

We also determined the power factor (PF)(23,51), which is an efficiency measure of the combined useful force generated. The power factor originates from the actuator disk model and the fact that force is proportional to the induced velocity squared, while power is proportional to the induced velocity cubed. PF was calculated as:

$PF = \frac{C_{Fuse}^{1.5}}{C_P}$. (10)

Finally, we computed the pitch torque resulting from the wing thrust. The moment arm used for the torque was computed as follows:

$h(t) = r_{rc} \cdot \sin(\theta(t))$, (11)

where θ is the flapping angle. We approximated the application point of the thrust along the wing to be located at a distance r_{rc} from the rotation point of the wing, defined as

$r_{rc} = \frac{\int_0^b r^2(b')c(b')db'}{\int_0^b r(b')c(b')db'}$, (12)

where *b* is the wingspan and *b'* is the spanwise position along the wing. This distance was weighed by the chord, as more force is produced where the wing is wider, and by the radius r from the rotation point, accounting for an increase of thrust towards the wing tips.
The flapping angle (θ) throughout the wingbeat was determined from the imposed kinematics. To synchronize the wing trajectory with the forces observed in the wake, we evaluated the relative shift within one sequence. We first selected a PIV sequence where the tip vortex was easily identifiable and manually selected the frame where it reached the lowest position. We then determined the frame where the wing was at the end of the downstroke in footage of the wing taken simultaneously to the PIV sampling. The delay between the PIV frame and the corresponding end of downstroke in the wing footage was then applied to every sequence, assuming that the different cases, given the fixed distance between wing and measurement plane and the constant tunnel speed, did not affect the time for the wake to travel from the wing to the PIV plane.
The moment was finally computed as

$M = T(t) \cdot h(t)$, (13)

and made dimensionless with

$$C_M = \frac{M}{q\bar{S}}, (14)$$

where $\bar{c} = S/b$ is the mean aerodynamic chord of the wing.

Statistics

To test for effects of the kinematic conditions we performed a GLM analysis (*fitglm* function with 'quadratic' model, Matlab R2025a, Mathworks Inc., USA), for each of the dependent variables with *TP* and *MWE* as independent, continuous, variables set to values –1, 0 and 1. Variation is given as standard error.

Results

Lift

The wingbeat average C_L varied non-linearly with both *TP* (*TP*: 0.0101±0.0044, p=0.0313; TP^2: -0.0331±0.0076, p=0.000286) and *MWE* (*MWE*: 0.1466±0.0044, p=33.3 1.14e^{-19}; MWE^2: -0.0664±0.0076, p=2.02e^{-08}). There was an increase in C_L with increasing *MWE*, regardless of *TP* (Fig. 1a). *TP*, per se, had a significant, but weak, effect on C_L, but there was a strong interaction effect between *TP* and *MWE* (*MWE***TP*: -0.1071±0.0054, p=4.25e^{-15}). When MWE was low, earlier TP reduced C_L, whereas when MWE was high, earlier TP increased C_L (Fig. 1a). When the *MWE* was zero the *TP* had little effect on C_L.

The instantaneous *L* over the wingbeat showed during which phases of the wingbeat we found differences between the treatments. In both the *TP* and *MWE* changes, a large proportion of the difference could be linked to the transition between the downstroke and the upstroke (Figs 2 and S3). Earlier *TP* and higher *MWE* both tended to increase C_L during this phase. At the transition between upstroke and downstroke we also found the curves diverging, but here the effects of the two kinematic variables differed. Earlier *TP* resulted in more negative lift, while higher *MWE* resulted in less negative C_L. We also found another effect of *MWE*, where C_L during the early and mid-downstroke was lower the higher the *MWE*.

Thrust

The wingbeat average C_T also varied with both *TP* and *MWE*. There was an increase in C_T with decreasing *MWE* (*MWE*: -0.0345±0.0037, p=6.58e^{-09}), regardless of *TP* (Fig. 1b). There was also a non-linear effect of *TP* on C_T (*TP*: 0.0631±0.0037, p=9.22e^{-14}; TP^2: -0.0439±0.0064, p=9.14e^{-07}), where C_T increased more the earlier the *TP*. There was no interaction effect between the two factors (p=0.11). Together this resulted in the lowest C_T was found when *MWE* was high and pitch happened early (Fig. 1b).

The instantaneous C_T over the wingbeat showed that later *TP* reduced negative C_T during the transition between downstroke and upstroke, but also lower C_T during the upstroke and downstroke transition (Figs 2 and S3). Lower *MWE* resulted in more C_T during the downstroke to upstroke transition.

Thrust to lift ratio

T/*L* indicates the direction of the force generated and results from a combination of the trends described above. *T*/*L* varied with both *TP* and *MWE*. There was a non-linear decrease in *T*/*L* with increasing *MWE* (*MWE*: -0.1342±0.0121, p=3.31e^{-10}; MWE^2: 0.0638±0.0210, p=0.0063), regardless of *TP* (Fig. 1c). There was also a non-linear increase of *T*/*L* with *TP* (*TP*: 0.0915±0.0121, p=2.14e^{-7}; TP^2: -0.0789±0.0210, p=0.0012). There was an interaction effect between the two factors (*MWE***TP*: 0.0496±0.0149, p=0.0032). Together this resulted in the lowest *T*/*L* found when *MWE* was high and pitch happened early (Fig. 1c).

Power

C_P varied linearly with *TP* (*TP*: -0.0459±0.0019, p=1.15e^{-16}) and non-linearly with *MWE* (*MWE*: 0.0117±0.0019, p=5.12e^{-06}; *MWE*^{2}: -0.0105±0.0034, p=0.00497) (Fig. 3a), while there was no significant interaction between *MWE* and *TP* (*MWE***TP*: p=0.0628). The earlier the pitch occurred the higher the C_P. For *MWE* there is weak increase in C_P with increasing *MWE*, but with a weak peak in C_P for the mid wing elevation.

Efficiency

PF varied linearly with *TP* (TP: 0.8681±0.0484, p=3.32e^{-14}) and non-linearly with *MWE* (*MWE*: 0.6532±0.0484, p=8.24e^{-12}; *MWE*^{2}: -0.3729±0.0839, p=0.00022) (Fig. 3b). There was a strong interaction effect (*MWE***TP*: -0.5256±0.0593, p=1.54e^{-08}) so that when *TP* occurred late *PF* increased strongly with increasing *MWE*, but when *TP* occurred early *PF* decreased with increasing *MWE* (or peaked at mid *MWE*).

COT varied non-linearly with *TP* (*TP*: -0.1418±0.0106, p=9.81e^{-12}; *TP*^{2}: 0.0469±0.0183, p=0.0185) and non-linearly with *MWE* (*MWE*: -0.1118±0.0106, p=7.76e^{-10}; *MWE*^{2}: 0.0740±0.0184, p=0.000611) (Fig. 3c). There was a strong interaction effect (*MWE***TP*: 0.1280±0.0130, p=2.53e^{-09}) so that *COT* was highest when *MWE* was low and *TP* occurred early and was lowest when *MWE* was high and *TP* occurred late.

Body pitch torque

We found the highest values of the pitch torque, C_M, acting on the body when the wing tip was the furthest from the center of the body (Fig. 4). This was the time during the wingbeat that the thrust had the greatest moment arm for pitch generation, but it also coincided with the phase of the wingbeat when we found peaks of thrust.

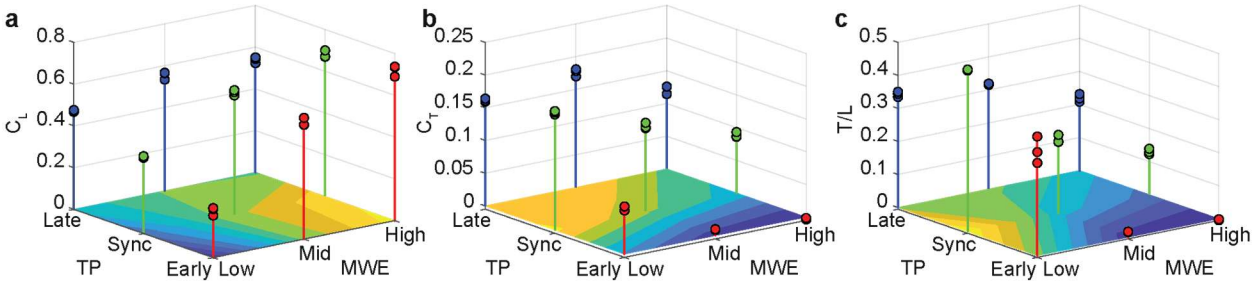

Figure 1: Average C_L and C_T throughout a wingbeat varies with timing of pitch (*TP*) and mean wing elevation (*MWE*). (a) C_L peaks when *MWE* is high and *TP* occurs early relative to the transition between down and upstroke, while it is minimum when *MWE* is low and *TP* occurs early relative to the transition between down and upstroke. (b) C_T peaks when the *MWE* is in the mid position and the *TP* occurs late relative to the transition between down and upstroke, while it is minimum when the *MWE* is high and *TP* occurs early relative to the transition between down and upstroke. (c) *T/L*

represents the direction of the force generated by the wing. Highest *T/L* is achieved when *MWE* is low and the *TP* is synchronized with the flapping motion, while the lowest *T/L* is found when *MWE* is high and *TP* is early.

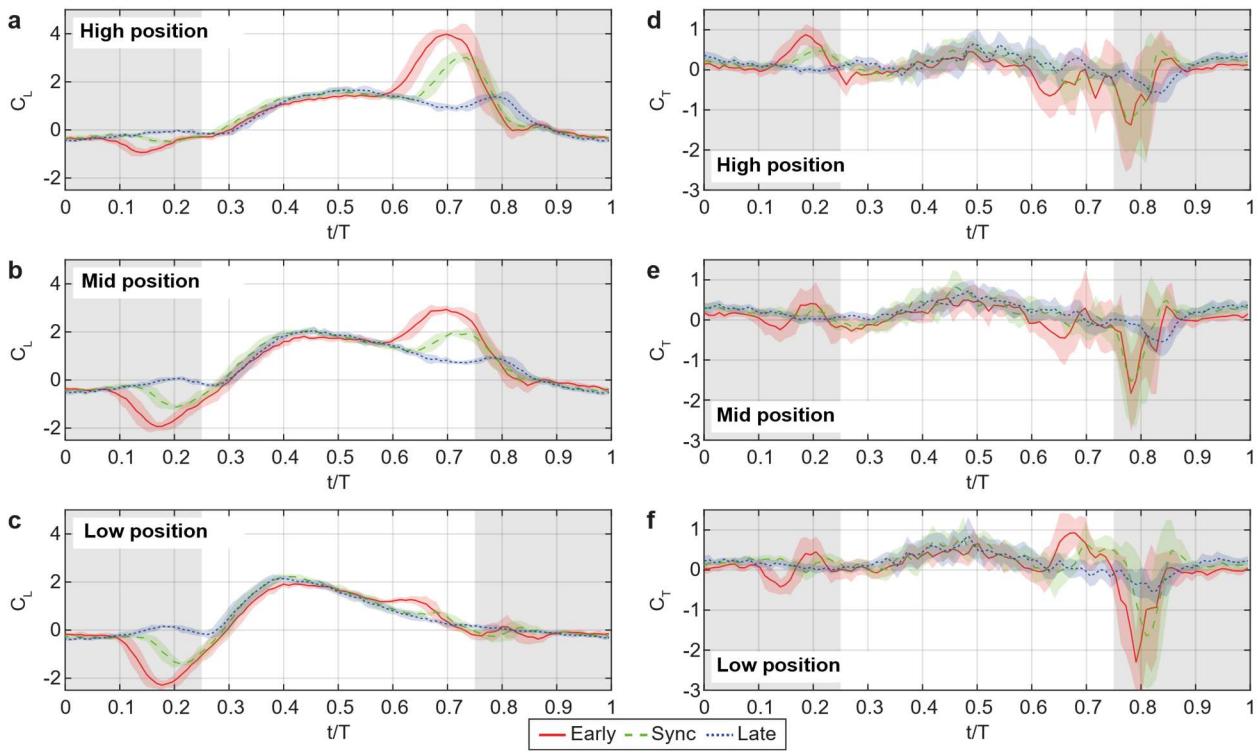

Figure 2: Instantaneous force coefficients through the flapping cycle. The left panels (**a-c**) show the impact on C_L and the right panels (**d-f**) show the impact on C_T for the timing of the pitch (*TP*) at different wing positions (*MWE* = High, Mid and Low). In each curve, the line represents the phase-averaged value over the three repeats and four wingbeats of each case, and the shaded area has a width of two standard deviations centered around the mean. Shaded background shows the upstroke.

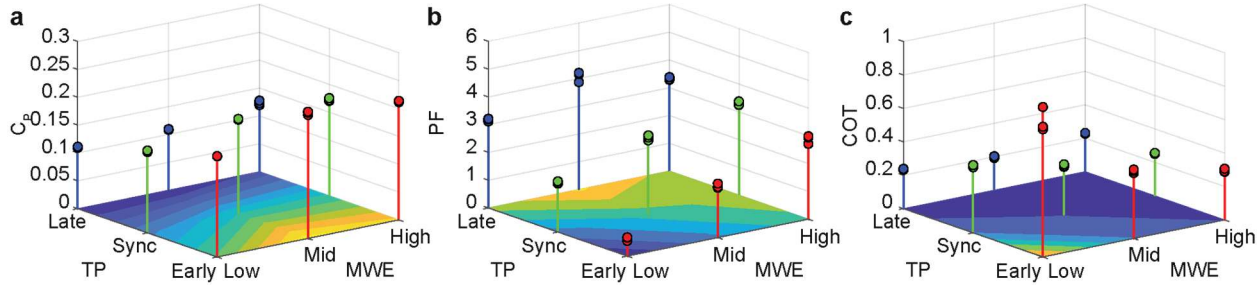

Figure 3: Aerodynamic power and efficiency vary with timing of pitch (*TP*) and mean wing elevation (*MWE*). (a) Power coefficient (C_P) varies strongly with *TP*, increasing the earlier the pitch occurs relative to the transition between downstroke and upstroke. There is also a generally lower C_P, the

lower the *MWE*. (b) Power factor (*PF*), a measure of the force/power generated, increases the later the *TP* occurs and the higher the *MWE* (except for the highest *MWE* with the latest *TP*). (c) Cost of transport (*COT*), the power/lift, is lowest when the *MWE* is high and *TP* occurs late and highest when the *MWE* is low and *TP* early.

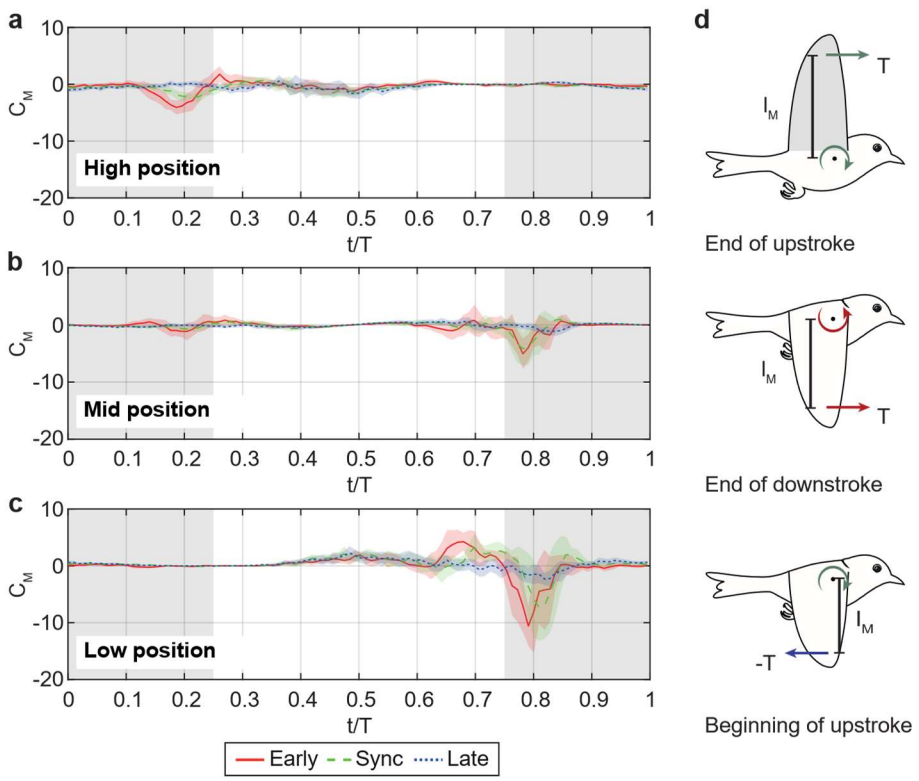

Figure 4: Pitch torque (C_M) acting on the body varied with kinematics. (a) When flapping the wing in the high position the thrust (*T*) generated during the upper turning point created a pitch down torque, while thrust generated at the lower turning point had little influence on C_M. (b) When the wing was in the mid position, *T* during both turning points results in increased C_M magnitude. (c) With the wing in the lower position, the lower turning point had a large impact on C_M, both during the end of the downstroke and the beginning of the upstroke. (d) Illustration of the moment arm (l_M) and *T* creating the pitch torque on the body during the turning phases of the wingbeat.

Discussion

Using a robotic wing to control individual aspects of how wings are flapped, we have shown that both the mean wing elevation (*MWE*) and the timing of wing pitch (*TP*) relative to the time of transitions between up- and down strokes can be used to determine the magnitude as well as the direction of the aerodynamic force generated. Interestingly, we also find interaction effects between *MWE* and *TP*, such that the response to the same *TP* varies with the *MWE*. Not only can adjusting these kinematic parameters control force magnitude and direction, but the efficiency of generating the forces is also affected. Depending on the goal of force generation – producing thrust

or generating weight support – different combinations of *MWE* and *TP* should be selected for best efficiency. This suggests a complexity, rarely considered, of the flight control mechanisms available to flying animals, but also novel mechanism to explore for controlling manmade flapping drones.

During flapping flight, the distance and angle between the wings vary throughout a wingbeat. When the wings are close, either above or below the body, they interact aerodynamically. This phenomenon is known as clap and fling in the extreme case that the wings touch during the turning point/transitions between up- and downstroke(52). The wings have mirror pressure distributions, which affect the aerodynamics of the wings, in a way similar to what happens during ground effect (42,43,46). When the wings move apart at the start of the downstroke, this results in a lower pressure between the wings than would be found on the wings operating on their own, which tends to increase lift (52,53). In our measurements, we find the expected decrease of the *T*/*L* ratio when the wings are high, but the extra lift mainly comes at the end of the downstroke rather than at the start (Fig. 2a). The main reason is probably that when the wings are in a high position, the downstroke ends in a position where the wing is closer to the horizontal plane and pitch up during this phase increases the angle of attack and the lift production. In addition, when the wings are high and the interaction effect between the wings is expected to be significant the force generated from each wing will be directed sideways, not contributing to the vertical force. When the wings come together at the end of the downstroke, when *MWE* is low, we instead get an increased pressure between the wings, which tends to increase the thrust generated by the wings. A recent study found that already a limited decrease of *MWE* increased the *T*/*L* ratio more than expected if the wing worked in solitude, which was attributed to a wing interaction at the end of the downstroke (30). Earlier studies on flapping flight in ground effect have suggested that how the wings are pitched when they interact with the surface affects the performance and explain the higher than predicted energy savings for bats (46) and modelled birds (54) during flapping flight in ground effect. We found that the amount of lift or thrust during the end of the downstroke depends on the pitch angle of the wings when they approach each other. If the leading edges of the wings meet first, as when using a delayed pitch, this results in more thrust than during the synchronized case. This is likely the result of the bottom, high pressure, wing surfaces being projected backwards during the transition between down and upstroke, which accelerates air backwards. If instead the trailing edges meet first, as when pitching up early, the forward projection of the high-pressure bottom wing surface would accelerate air forwards, which is reflected in negative thrust during this phase (Fig. 2). Our results thus support the notion that the attitude of the wings during the interaction makes a significant impact on the outcome of the interaction.

An interesting finding is that both the *PF* and *COT* suggest that the most efficient flight happens when we have a late *TP* and *MWE* is in the mid or high position. Looking at the components of these efficiency measures we see that this is to a large extent driven by a low *CP* for late *TP* and relatively high force generation (C_L and C_T). A consequence of this result is that unless necessary for force balance or maneuver/stability reasons, we would expect animals to flap their wings relatively symmetrical around the horizontal plane. To maximize C_L, flapping the wings high and with an early *TP* gives the highest output, while for maximizing C_T the wing should be in a mid to low position with a synchronized or late *TP*. If the goal is to change the direction of the force generated (i.e. *T*/*L*), a high wing position with an early *TP* tilts the force upwards the most and a low wing position with a synced *TP* tilts the force forwards the most. This means that simple, but relatively understudied,

kinematic changes can be used to control flight. Depending on what to achieve, different flapping strategies can be seen to be optimal. One of the key factors with the parameters we have studied here is that they, in addition to being allowed to vary between wingbeats, can be adjusted within a single wingbeat (Fig. 2). Thereby they give a rapid response to changing conditions or goals. A prediction based on these findings is that we will be likely to find large variation in how animals generate maneuvers or stabilize flight, depending on the phase of the wingbeat they decide to adjust their trajectory. This will at least apply to animals with relatively low wingbeat frequency compared to the speed of their control system (sensors and processing), such as birds and bats, that would benefit relatively more from course corrections within wingbeats. Indeed, one of the few studies looking at the aerodynamics of maneuvers actually used by animals have showed a variety of mechanisms (including varying the *MWE* of the left and right wing separately) in bats, depending on the phase of the wingbeat when the maneuver is initiated (10).

Another flight control mechanism, which is linked to the transition phases, involves the relatively large variation in thrust when we change the *TP*. Modulating thrust during the phases when the wings reach their most elevated or most depressed positions provides an effective means of controlling body pitch. Changes in the *MWE* simultaneously alter both the magnitude of thrust, through modifications to wing–wing aerodynamic interactions, and the moment arm of this force, by shifting the vertical position of the wings at the phase when thrust is produced. Together, these effects determine the pitch torque acting on the body. This mechanism thus provides a tailless pitch control that can be used to stabilize flight when flying without a tail (37), but also to initiate maneuvers (55). In addition, it is possible to generate yaw torques by employing different *TP* strategies for the left and right wings, while left–right asymmetries in *MWE* can be used to produce roll torques (10,56). These control strategies can then be applied in concert with other mechanism, including active wing morphing (57,58), resulting in a flexible control mechanism that can be applied within a single wingbeat and with a short response time. Understanding how different species utilize these mechanisms to achieve maneuvers, depending on wingbeat phase and strength of the maneuver, represents an exciting avenue for future research.

Conclusion

Our results demonstrate that previously overlooked kinematic strategies can substantially influence the direction, magnitude, and efficiency of aerodynamic forces generated by flapping wings. Both mean wing elevation and the timing of wing pitch independently affect aerodynamic performance, but notably, we also uncover a strong interaction between them. This suggests that these two kinematic parameters can be combined to enhance force production or improve efficiency in ways not achievable through either parameter alone. Moreover, we show that these kinematic adjustments determine when thrust is produced within the wingbeat, thereby modulating the pitch torque acting on the body, a tailless mechanism that animals could exploit to stabilize flight or initiate maneuvers. Together, these findings highlight the need for more detailed examinations of wing kinematics to understand how flying animals achieve such precise control, while also revealing new control strategies that could inform the design of manmade flapping-wing systems.

Acknowledgement

The research was funded by grants from the Crafoord foundation (20170584) and the Swedish Research Council (2017-03890 and 2022-02850 to L.C.J.). The PIV equipment was financed by an infrastructure grant from Lund University (https://www.lu.se/) to Anders Hedenström, Per Henningsson and L.C.J..

References

1. Skandalis DA, Baliga VB, Goller B, Altshuler DL. The spatiotemporal richness of hummingbird wing deformations. J Exp Biol. 2024 May 21;227(10):jeb246223. doi:10.1242/jeb.246223

2. Aldridge HD. Kinematics and aerodynamics of the greater horseshoe bat, *Rhinolophus ferrumequinum* , in horizontal flight at various flight speeds. J Exp Biol. 1986 Nov 1;126(1):479–97. doi:10.1242/jeb.126.1.479

3. Henningsson P, Spedding GR, Hedenström A. Vortex wake and flight kinematics of a swift in cruising flight in a wind tunnel. J Exp Biol. 2008 Mar 1;211(5):717–30. doi:10.1242/jeb.012146

4. Hubel TY, Riskin DK, Swartz SM, Breuer KS. Wake structure and wing kinematics: the flight of the lesser dog-faced fruit bat, *Cynopterus brachyotis*. J Exp Biol. 2010 Oct 15;213(20):3427–40. doi:10.1242/jeb.043257

5. Tobalske BW, Hedrick TL, Biewener AA. Wing kinematics of avian flight across speeds. J Avian Biol. 2003 Jun;34(2):177–84. doi:10.1034/j.1600-048X.2003.03006.x

6. Tobalske BW, Warrick DR, Clark CJ, Powers DR, Hedrick TL, Hyder GA, et al. Three-dimensional kinematics of hummingbird flight. J Exp Biol. 2007 Jul 1;210(13):2368–82. doi:10.1242/jeb.005686

7. Tobalske BW, Dial KP. Flight Kinematics of Black-Billed Magpies and Pigeons Over a Wide Range of Speeds. J Exp Biol. 1996 Feb 1;199(2):263–80. doi:10.1242/jeb.199.2.263

8. Von Busse R, Hedenström A, Winter Y, Johansson LC. Kinematics and wing shape across flight speed in the bat, *Leptonycteris yerbabuenae*. Biol Open. 2012 Dec 15;1(12):1226–38. doi:10.1242/bio.20122964

9. Hedrick TL, Biewener AA. Low speed maneuvering flight of the rose-breasted cockatoo (*Eolophus roseicapillus*). I. Kinematic and neuromuscular control of turning. J Exp Biol. 2007 Jun 1;210(11):1897–911. doi:10.1242/jeb.002055

10. Henningsson P, Jakobsen L, Hedenström A. Aerodynamics of manoeuvring flight in brown long-eared bats (Plecotus auritus). J R Soc Interface. 2018;15(148):20180441. doi:10.1098/rsif.2018.0441

11. Iriarte-Díaz J, Swartz SM. Kinematics of slow turn maneuvering in the fruit bat *Cynopterus brachyotis*. J Exp Biol. 2008 Nov 1;211(21):3478–89. doi:10.1242/jeb.017590

12. Warrick DR, Dial KP. Kinematic, Aerodynamic and Anatomical Mechanisms in the Slow, Maneuvering Flight of Pigeons. J Exp Biol. 1998 Mar 1;201(5):655–72. doi:10.1242/jeb.201.5.655

13. Chen Z(陈增爽), Xie Y(谢雨馨), Zhang Y(张扬), Li L(李立), Meng X(孟雪广). Aerodynamics of a flapping wing with stroke deviation in forward flight. Phys Fluids. 2024 May 15;36(5):051908. doi:10.1063/5.0209169

14. Dickinson MH, Lehmann FO, Sane SP. Wing Rotation and the Aerodynamic Basis of Insect Flight. Science. 1999 Jun 18;284(5422):1954–60. doi:10.1126/science.284.5422.1954

15. Harvey C, de Croon G, Taylor GK, Bomphrey RJ. Lessons from natural flight for aviation: then, now and tomorrow. J Exp Biol. 2023 Apr 17;226(Suppl_1):jeb245409. doi:10.1242/jeb.245409

16. Chin DD, Lentink D. Flapping wing aerodynamics: from insects to vertebrates. J Exp Biol. 2016 Apr 1;219(7):920–32. doi:10.1242/jeb.042317

17. Hedenström A, Johansson LC. Bat flight: aerodynamics, kinematics and flight morphology. J Exp Biol. 2015 Mar 1;218(5):653–63. doi:10.1242/jeb.031203

18. Liu H, Wang S, Liu T. Vortices and Forces in Biological Flight: Insects, Birds, and Bats. Annu Rev Fluid Mech. 2024 Jan 5;56(1):annurev-fluid-120821-032304. doi:10.1146/annurev-fluid-120821-032304

19. Swartz SM, Konow N. Advances in the study of bat flight: the wing and the wind. Can J Zool. 2015 Dec;93(12):977–90. doi:10.1139/cjz-2015-0117

20. Tobalske BW. Aerodynamics of avian flight. Curr Biol. 2022 Oct 24;32(20):R1105–9. doi:10.1016/j.cub.2022.07.007 PubMed PMID: 36283374.

21. Kwon HK, Chang JW. Effects of shapes and kinematics of hovering flapping wings on aerodynamic forces and vortex structures. Sci Rep. 2025 Feb 13;15(1):5098. doi:10.1038/s41598-025-86113-9

22. Lang X, Song B, Yang W, Yang X, Xue D. Sensitivity Analysis of Wing Geometric and Kinematic Parameters for the Aerodynamic Performance of Hovering Flapping Wing. Aerospace. 2023 Jan 10;10(1):74. doi:10.3390/aerospace10010074

23. Lentink D, Dickinson MH. Rotational accelerations stabilize leading edge vortices on revolving fly wings. J Exp Biol. 2009 Aug 15;212(16):2705–19. doi:10.1242/jeb.022269

24. Sane SP, Dickinson MH. The aerodynamic effects of wing rotation and a revised quasi-steady model of flapping flight. J Exp Biol. 2002;205:1087–96. doi:10.1242/jeb.205.8.1087

25. Guerrero JE. Wake Signature and Strouhal Number Dependence of Finite-Span Flapping Wings. J Bionic Eng. 2010 Sep 1;7:S109–22. doi:10.1016/S1672-6529(09)60224-9

26. Johnson KC, Thurow BS, Wabick KJ, Berdon RL, Buchholz JHJ. Vortex topology of a pitching and rolling wing in forward flight. Exp Fluids. 2020 Oct 1;61(10):221. doi:10.1007/s00348-020-03048-9

27. Nadig SV, Ghosh S. Lift enhancement via leading edge vortex delay in flapping flight utilizing kinematic modifications. Phys Fluids. 2024 Nov 15;36(11):115168. doi:10.1063/5.0236826

28. Xue D, Liu J, Zhang B, Song B. A universal law for predicting the thrust performance of flapping thin airfoils. Phys Fluids. 2025 Jul 24;37(7):071919. doi:10.1063/5.0276982

29. Parslew B. Predicting Trends in Avian Wing Motion and Energetics Across Scales [Internet]. bioRxiv; 2025 [cited 2025 Jul 28]. p. 2025.06.10.658879. Available from: https://www.biorxiv.org/content/10.1101/2025.06.10.658879v2 doi:10.1101/2025.06.10.658879

30. Johansson LC. Aerodynamic efficiency explains flapping strategies used by birds. Proc Natl Acad Sci. 2024 Nov 12;121(46):e2410048121. doi:10.1073/pnas.2410048121

31. Deetjen ME, Chin DD, Heers AM, Tobalske BW, Lentink D. Small deviations in kinematics and body form dictate muscle performances in the finely tuned avian downstroke. Watanabe YY, Rutz C, editors. eLife. 2024 Feb 26;12:RP89968. doi:10.7554/eLife.89968

32. Ingersoll R, Haizmann L, Lentink D. Biomechanics of hover performance in Neotropical hummingbirds versus bats. Sci Adv. 2018 Sep 26;4(9):eaat2980. doi:10.1126/sciadv.aat2980

33. Moriche M, Flores O, García-Villalba M. On the aerodynamic forces on heaving and pitching airfoils at low Reynolds number. J Fluid Mech. 2017 Oct 10;828:395–423. doi:10.1017/jfm.2017.508

34. Park KJ, Rosén M, Hedenström A. Flight kinematics of the barn swallow (*Hirundo rustica*) over a wide range of speeds in a wind tunnel. J Exp Biol. 2001 Aug 1;204(15):2741–50. doi:10.1242/jeb.204.15.2741

35. Rosén M, Spedding GR, Hedenström A. Wake structure and wingbeat kinematics of a house-martin *Delichon urbica*. J R Soc Interface. 2007 Aug 22;4(15):659–68. doi:10.1098/rsif.2007.0215

36. Rosén M, Spedding GR, Hedenström A. The relationship between wingbeat kinematics and vortex wake of a thrush nightingale. J Exp Biol. 2004;207:4255–68. doi:10.1242/jeb.01283

37. Johansson LC, Hedenström A. The vortex wake of blackcaps (*Sylvia atricapilla* L.) measured using high-speed digital particle image velocimetry (DPIV). J Exp Biol. 2009 Oct 15;212(20):3365–76. doi:10.1242/jeb.034454

38. Wolf M, Johansson LC, Von Busse R, Winter Y, Hedenström A. Kinematics of flight and the relationship to the vortex wake of a Pallas' long tongued bat (*Glossophaga soricina*). J Exp Biol. 2010 Jun 15;213(12):2142–53. doi:10.1242/jeb.029777

39. Hubel TY, Hristov NI, Swartz SM, Breuer KS. Changes in kinematics and aerodynamics over a range of speeds in *Tadarida brasiliensis* , the Brazilian free-tailed bat. J R Soc Interface. 2012 Jun 7;9(71):1120–30. doi:10.1098/rsif.2011.0838

40. Ajanic E, Paolini A, Coster C, Floreano D, Johansson C. Robotic Avian Wing Explains Aerodynamic Advantages of Wing Folding and Stroke Tilting in Flapping Flight. Adv Intell Syst. 2023 Feb;5(2):2200148. doi:10.1002/aisy.202200148

41. Pennycuick CJ, Alerstam T, Hedenström A. A new low-turbulence wind tunnel for bird flight experiments at Lund University, Sweden. J Exp Biol. 1997;200:1441–9. doi:10.1242/jeb.200.10.1441

42. Lighthill J. A simple fluid-flow model of ground effect on hovering. J Fluid Mech. 1979 Aug;93(04):781. doi:10.1017/S0022112079002032

43. Rayner JMV. On the aerodynamics of animal flight in ground effect. Phil Trans R Soc Lond B. 1991;334:119–28.

44. Percin M, Hu Y, van Oudheusden BW, Remes B, Scarano F. Wing Flexibility Effects in Clap-and-Fling. Int J Micro Air Veh. 2011 Dec 1;3(4):217–27. doi:10.1260/1756-8293.3.4.217

45. Quinn DB, Moored KW, Dewey PA, Smits AJ. Unsteady propulsion near a solid boundary. J Fluid Mech. 2014 Mar 10;742:152–70. doi:10.1017/jfm.2013.659

46. Johansson LC, Jakobsen L, Hedenström A. Flight in Ground Effect Dramatically Reduces Aerodynamic Costs in Bats. Curr Biol. 2018 Nov;28(21):3502-3507.e4. doi:10.1016/j.cub.2018.09.011

47. Tong W, Yang Y, Wang S. Estimating thrust from shedding vortex surfaces in the wake of a flapping plate. J Fluid Mech. 2021 Aug 10;920:A10. doi:10.1017/jfm.2021.434

48. Von Busse R, Waldman RM, Swartz SM, Voigt CC, Breuer KS. The aerodynamic cost of flight in the short-tailed fruit bat (*Carollia perspicillata*): comparing theory with measurement. J R Soc Interface. 2014 Jun 6;11(95):20140147. doi:10.1098/rsif.2014.0147

49. Johansson LC, Maeda M, Henningsson P, Hedenström A. Mechanical power curve measured in the wake of pied flycatchers indicates modulation of parasite power across flight speeds. J R Soc Interface. 2018 Jan;15(138):20170814. doi:10.1098/rsif.2017.0814

50. Drela M. Power Balance in Aerodynamic Flows. AIAA J. 2009 Jul;47(7):1761–71. doi:10.2514/1.42409

51. Wang ZJ. Aerodynamic efficiency of flapping flight: analysis of a two-stroke model. J Exp Biol. 2008 Jan 15;211(2):234–8. doi:10.1242/jeb.013797

52. Weis-Fogh T. Quick estimates of flight fitness in hovering animals, including novel mechanisms for lift production. J Exp Biol. 1973;59:169–230. doi:10.1242/jeb.59.1.169

53. Maxworthy T. Experiments on the Weis-Fogh mechanism of lift generation by insects in hovering flight. Part 1. Dynamics of the 'fling'. J Fluid Mech. 1979 Jul 12;93(1):47–63. doi:10.1017/S0022112079001774

54. Su JY, Tang JH, Wang CH, Yang JT. A numerical investigation on the ground effect of a flapping-flying bird. Phys Fluids. 2013 Sep 1;25(9):093101. doi:10.1063/1.4819503

55. Lee EH, Yang HH, Lee SG, Han JH. A Biologically-Inspired Flapping-Wing Air Vehicle With Active Folding-Wings. IEEE Robot Autom Lett. 2026 Mar;11(3):2786–93. doi:10.1109/LRA.2026.3653275

56. Anuar K, Amemiya A, Sato H, Afakh ML, Yunanto B, Mochiyama H, et al. Agile Maneuvering of Servo-Driven Flapping Robot: Novel Approach Using Center Flapping Angle and Offset Angle Variables. IEEEASME Trans Mechatron. 2026;1–12. doi:10.1109/TMECH.2025.3648513

57. Ajanic E, Feroskhan M, Wüest V, Floreano D. Sharp turning maneuvers with avian-inspired wing and tail morphing. Commun Eng. 2022 Nov 24;1(1):34. doi:10.1038/s44172-022-00035-2

58. Chang E, Chin DD, Lentink D. Bird-inspired reflexive morphing enables rudderless flight. Sci Robot. 2024 Nov 20;9(96):eado4535. doi:10.1126/scirobotics.ado4535

Supplemental information

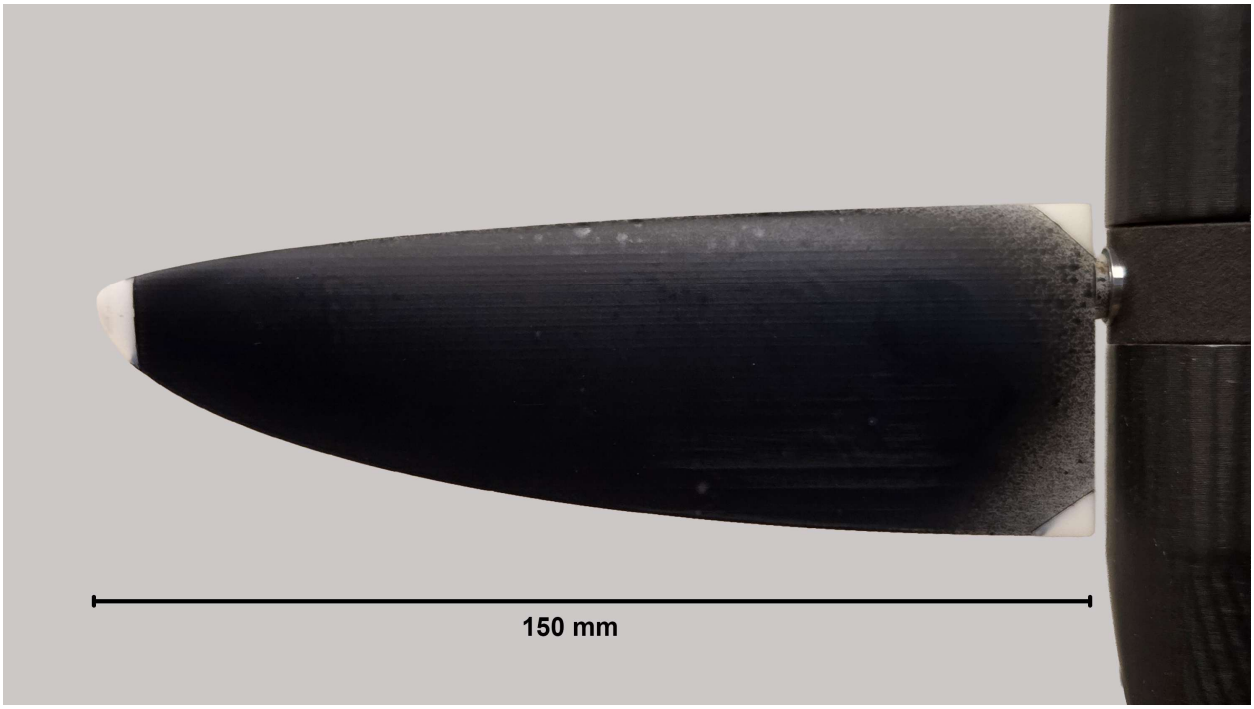

Figure S1. Wing used on the robot.

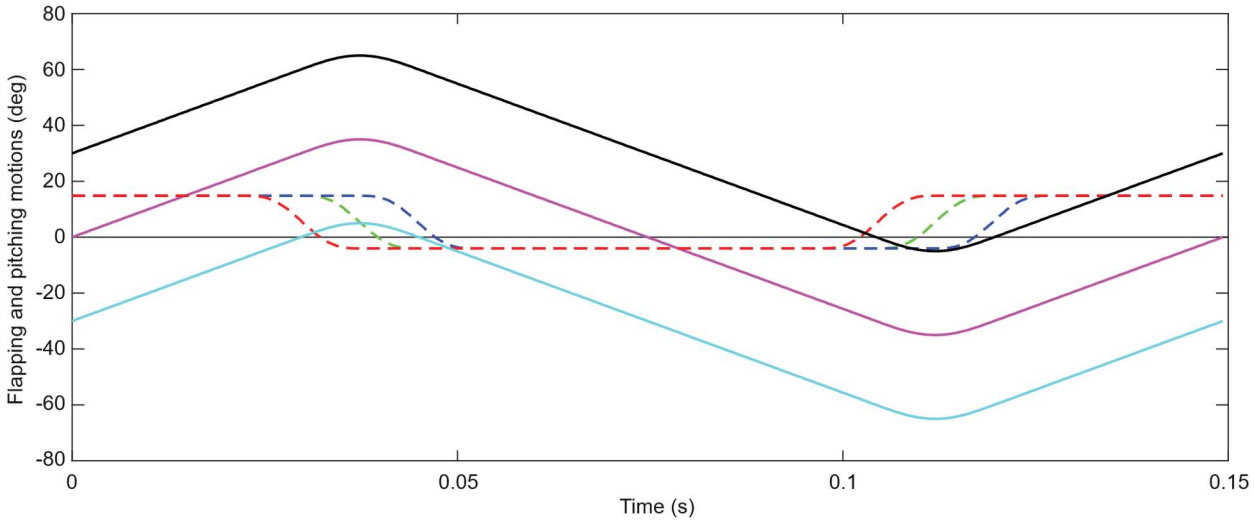

Figure S2. Temporal variation in flapping angle (black-high, magenta-mid and cyan-low) and pitching angle (red-early, green-synchronized and blue-late) over time.

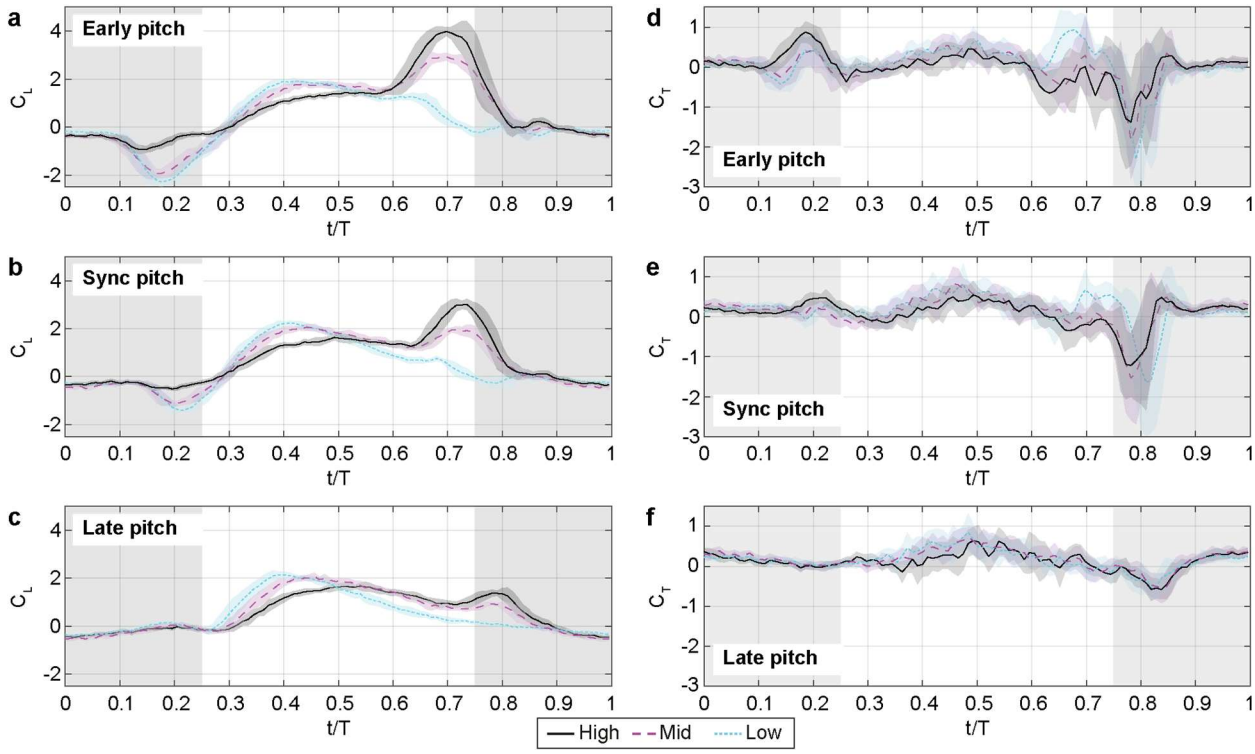

Figure S3. Instantaneous force coefficients through the flapping cycle. The left panels (**a-c**) show the impact on C_L and the right panels (**d-f**) show the impact on C_T for the different wing positions (*MWE* = High, Mid and Low) for each of the timing of the pitch (*TP* = Early, Sync and Late). In each curve, the line represents the phase-averaged value over the three repeats and four wingbeat of each case, and the shaded area has a width of two standard deviations centered around the mean. The data is the same as in Fig. 2 but divided in the alternate way to facilitate interpretation. Shaded background indicates the upstroke.

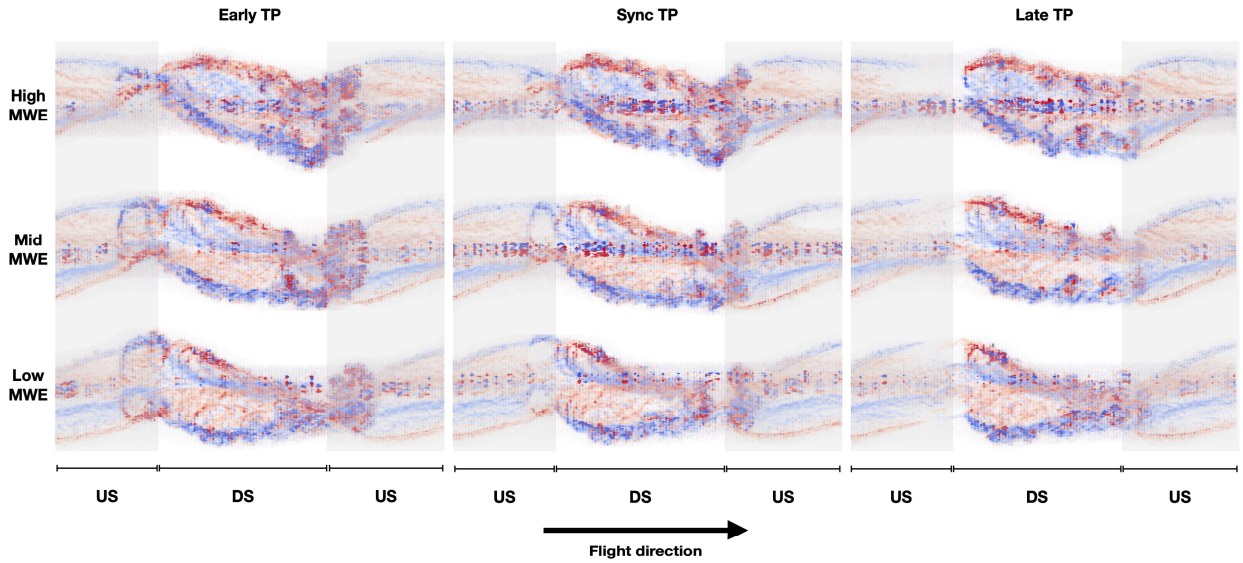

Figure S4. Volume rendering of the reconstructed vorticity field for one of each tested case. The magnitude of the vorticity vector is used for the rendering, and it is colored towards red or blue depending on the sign of the streamwise component of the vorticity. The upstrokes are highlighted with shaded areas.